Concluding destructive investigation of a nine-year-old marine-exposed cracked concrete panel

Cement and Concrete Research 165 (2023) 107070

Contents lists available at ScienceDirect

Cement and Concrete Research

journal homepage: www.elsevier.com/locate/cemconres

Concluding destructive investigation of a nine-year-old marine-exposed cracked concrete panel

Mette Geiker [a,*], Samanta Robuschi [b], Karin Lundgren [b], Charilaos Paraskevoulakos [c], Carsten Gundlach [d], Tobias Danner [e], Ulla Hjorth Jakobsen [f], Alexander Michel [c]

[a] Norwegian University of Science and Technology (NTNU), Department of Structural Engineering, Trondheim, Norway
[b] Chalmers University of Technology, Division of Structural Engineering, Sweden
[c] Technical University of Denmark (DTU), Department of Civil Engineering, Lyngby, Denmark
[d] Technical University of Denmark (DTU), DTU Physics, Lyngby, Denmark
[e] SINTEF Building and Infrastructure, Trondheim, Norway
[f] Danish Technological Institute (DTI), Taastrup, Denmark

ARTICLE INFO

Keywords:
Reinforced concrete
Cracks
Characterization
In-situ marine exposure
Reinforcement corrosion

ABSTRACT

This study undertaken on a nine-year-old cracked concrete panel further investigates the impact of cracks on the corrosion performance of conventional steel reinforcement in marine-exposed concrete to explain observed monitoring data. The present data covers seven 1.80 m long (12.6 m) reinforcing bars embedded in good quality concrete (w/b = 0.40 and cover >75 mm). Each bar was crossed by two horizontal cracks (surface crack widths 0.20–0.30 mm). The investigation showed no corrosion on the surface of the reinforcing bars, in either cracked or uncracked areas. Two of the seven reinforcing bars were instrumented in the vicinity of the cracks. Extensive corrosion was found in the interior of all instrumented parts of these bars. This may explain the monitoring data despite the lack of corrosion on the exterior surface of the two instrumented rebars. However, with no other weaknesses, the remaining conventional rebars showed no impact from the cracks.

1. Introduction

The corrosion of steel reinforcing bars is the most common cause of deterioration in reinforced concrete structures. Regulating concrete cover quality (i.e., its denseness and thickness) and surface crack width has been the preferred strategy for preventing corrosion damage for many years. Depending on the environmental class defined, e.g., by the presence of chlorides and moisture conditions, different crack width limits apply. However, these requirements can be questioned, because the effect of cracks on durability is debated among researchers.

It is generally accepted that transversal cracks reduce the time to corrosion initiation, which is explained by the rapid ingress of aggressive substances [1]. However, observations that contradict this have been made on the long-term impact of transverse cracks on the propagation of reinforcement corrosion [2]. The development of corrosion appears to be more affected by the concrete cover quality and thickness than the surface crack width [3,4]. Some researchers have suggested that the maximum steel stress (which affects the crack width at the reinforcement) is more critical for corrosion behaviour than the maximum surface crack width [5,6]. Papakonstantinou and Shinozuka [7] suggest that self-healing might explain why cracks with small widths do not affect long-term corrosion. Another possible explanation for the observations on the long-term impact of cracks is that other and more pronounced weaknesses may override the corrosion impact of the presence of cracks [8].

This work presents the results from a field exposure experiment. A 2.00 m × 1.00 m × 0.20 m panel was cast in the laboratory from Portland cement concrete with a water-to-binder ratio of 0.40 and large cover thickness (>75 mm), exposed for nine years at the Rødbyhavn field exposure site owned by Femern Bælt A/S in Denmark. Initially, the panel was cured sealed for approximately 70 maturity days. Then two bending (tapered) cracks with similar surface crack widths (0.20–0.30 mm) were introduced, after which the specimen was stored seven months onsite still sealed in plastic until exposure. The panel was

* Corresponding author.
E-mail addresses: mette.geiker@ntnu.no (M. Geiker), samanta.robuschi@norconsult.com (S. Robuschi), Karin.Lundgren@chalmers.se (K. Lundgren), chapa@byg.dtu.dk (C. Paraskevoulakos), cagu@fysik.dtu.dk (C. Gundlach), tobias.danner@sintef.no (T. Danner), uhj@teknologisk.dk (U.H. Jakobsen), almic@byg.dtu.dk (A. Michel).

https://doi.org/10.1016/j.cemconres.2022.107070
Received 2 June 2022; Received in revised form 12 December 2022; Accepted 19 December 2022
Available online 26 January 2023

Table 1
Concrete composition.

Constituent	[kg/m^3]
Cement	368.5
Water	143.3
Fine aggregates (0–2 mm)	699.6
Coarse aggregates (4–8 mm)	379.8
Coarse aggregates (8–16 mm)	267.5
Coarse aggregates (16–22 mm)	532.2
Air entraining agent	1.7
Superplasticizer	3.0
Total	2395.7
Free water	147.0
w/c-ratio [−]	0.4
Air content [%]	3.8

positioned at the exposure site with the cracks orientated horizontally. One of the cracks was exposed fully submerged, while the other was in the tidal zone. The panel was instrumented with multi-ring electrodes for depth-dependent temperature and resistivity monitoring, and two custom-made rebars were instrumented to monitor the open circuit potential (OCP) in the vicinity of the cracks. The instrumented rebars contained small pins, spaced out approximately every 10 mm and electrically isolated from each other. Michel et al. [9] presented and discussed monitoring data for the first seven years of exposure. Their results indicated that active corrosion initiated after almost two years of exposure. This observation contrasts with many laboratory investigations that report rapid corrosion initiation in cracked concrete [10–15]. Moreover, Michel et al. [9] observed cyclic OCP behaviour, indicating depassivation and repassivation of the pins. The pin sensors in both the tidal and submerged zones indicated that apparent active corrosion continued to a varying extent for periods of approximately one and a half years.

The aim of this study was to investigate further the impact of cracks on the corrosion performance of conventional steel reinforcement in marine-exposed cracked concrete and to explain the observed monitoring data. The panel contained seven vertically positioned reinforcing bars, five conventional and two instrumented. The instrumented rebars were custom-made and earlier successfully used for short-term laboratory studies [10]. The reinforcing bars were electrically isolated from each other. After nine years of exposure, cores (ø100 mm) were drilled in cracked areas of the three middle bars (one conventional and two instrumented) for detailed crack morphology and composition analysis using visual inspection, X-ray micro-computed tomography (μ-CT), micro X-ray fluorescence spectrometry (μ-XRF), and petrography. The remaining reinforcement was excavated for the identification of any corrosion there might be.

The investigation showed no corrosion on the surface of the reinforcing bars, in either cracked or uncracked areas. Extensive corrosion was found in the interiors of all four instrumented rebar parts and could protect the non-corroding steel surfaces and thus explain the lack of corrosion spots on the outer steel surface in contact with the concrete; however, the remaining conventional rebars showed no corrosion impact from the cracks nor any other weaknesses.

The apparently periodical corrosion activity identified by monitoring OCP during the first seven years of exposure [9] can be explained by extensive corrosion inside the instrumented reinforcing bars and on the interior of the pins. This might be due to unintended ingress along cables and shows that the design of the instrumented reinforcing bars needs to be adjusted if used for long-term monitoring.

2. Experimental

The experimental study investigated a cracked reinforced concrete panel made from plain Portland cement after nine years of marine exposure, from June 2011 to October 2020.

2.1. Concrete panel

The reinforced concrete panel was prepared from plain Portland cement with a water-to-cement ratio of 0.40. Table 1 gives the mix composition, while the oxide composition of the cement can be found in Table 2. The panel dimensions were 1.00 m × 2.00 m × 0.20 m (length × height × width) with seven vertical reinforcing bars embedded in the concrete: five conventional reinforcing bars with a diameter of 12 mm and two custom-made instrumented reinforcing bars with a diameter of 25 mm, see Fig. 1. The custom-made instrumented reinforcing bars contained approximately 300 mm long hollowed sections with 17 drilled holes. A steel pin was mounted in an insulating sheath in each of these holes to allow for individual electrochemical potential and corrosion current measurements. All electrical connections to the individual pins were threaded through the hollow section. More information can be found in Michel et al. [9]. The reinforcing bars were centrally positioned, resulting in 94.0 mm and 87.5 mm cover thicknesses for the conventional and instrumented reinforcing bars, respectively. All reinforcing bars were mounted on horizontal composite bars to ensure that the individual steel bars (whether conventional or instrumented) were electrically disconnected from each other.

The concrete was mixed and cast at the Danish Technological Institute. Mixing was carried out using a concrete mixing plant with a 250 L capacity. Homogenization of the individually prepared concrete batches was ensured using a 500 L pan mixer. Concrete casting was undertaken from the top of the formwork resulting in a maximum drop height of approximately 2.20 m. The concrete was cast in five subsequent layers, and each layer was compacted individually using a small poker vibrator. After casting, the form was stored at laboratory conditions (i.e., 18 ± 2 °C) and covered with plastic for 48 h. Upon demoulding, the panel was cured sealed in plastic under laboratory conditions for an additional 68 days.

Subsequently and before exposure, two cracks were mechanically introduced in the panel by means of three-point bending. The cracks were located approximately 0.70 m (Crack 1, tidal exposure) and 1.50 m (Crack 2, submerged exposure) from the top of the panel, see Fig. 1. A DEMEC Mechanical Strain Gauge was used to measure crack width in both locations (for three pairs of measuring points along the crack path) both during the cracking and after 1.5 years. Upon cracking, two recesses of approximately 10 cm × 5 cm × 5 cm (length × width × depth) were cut at the edges and along the crack path of the panel. Subsequently, the recesses were filled with fast-hardening repair mortar to retain induced crack widths (see Table 3). The repair mortar was allowed to cure sealed for 24 h before maintaining the applied load and, thus, the crack widths. Then the specimen was stored for seven months onsite still sealed in plastic until exposure.

2.2. Exposure

The panel was exposed to seawater at an exposure site in the Rødbyhavn area in Denmark. The chloride content of the seawater there is approximately 0.70 % (7.0 g/L) [17], and annual temperature variations of the seawater typically range from −1 to 20 °C. The specimen was partly immersed in the seawater, with the upper 0.70 m above the mean

Table 2
Oxide composition of cement; after [16].

	CaO	SiO_2	Al_2O_3	Fe_2O_3	SO_3	MgO	TiO_2	P_2O_5	CO_2	LOI	Na_2O
Mass %	65.6	24.8	2.9	2.3	2.2	0.8	0.1	0.2	0.2	0.7	0.7

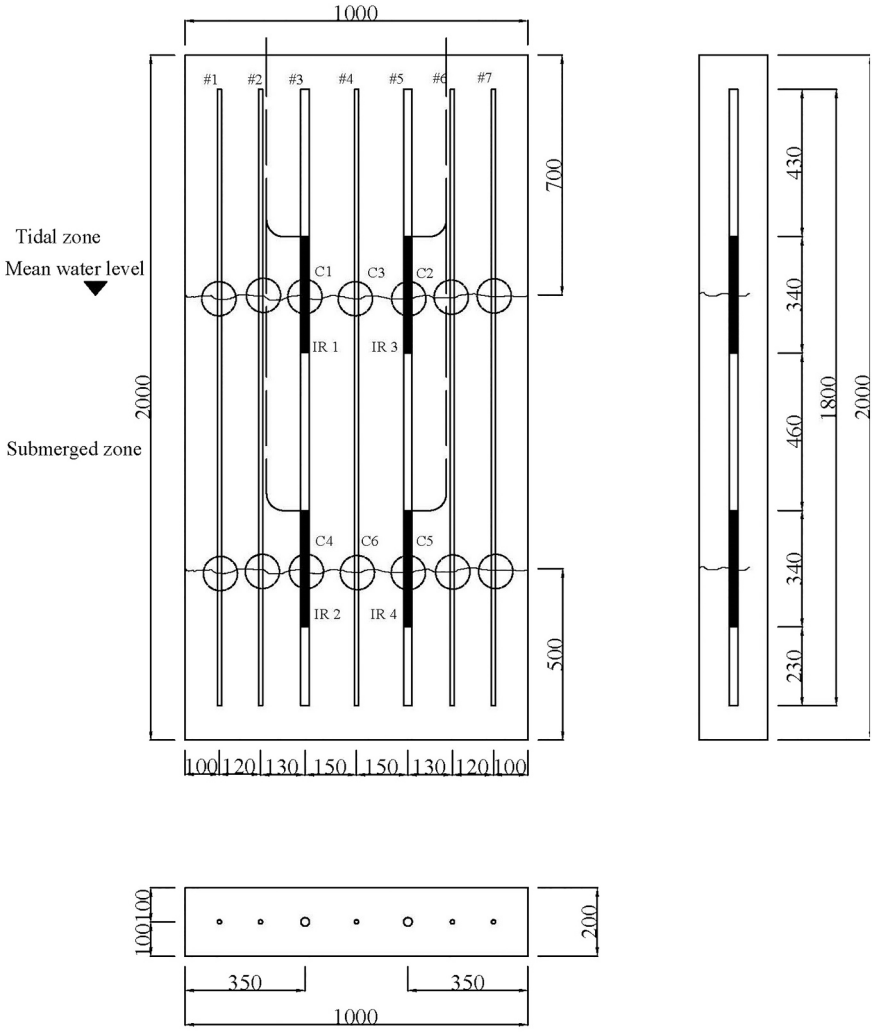

Fig. 1. Dimensions of the panel, location of mean water level, the two horizontal cracks, and cores extracted for this study: Series 1: cores C3 and C6 include parts of conventional reinforcing bars, cores C1, C2, C4 and C5 include parts of instrumented reinforcing bars; Series 2: numbering of cores. #1–7, numbering of rebar sections: IR 1–4, instrumented rebars: #3 and #5. All measures in mm.

Table 3
Surface crack width in (mm) before and during early exposure of the panel. The three measuring points were distributed approximately evenly along the crack path.

	Crack 1 0.70 m from top, tidal exposure			Crack 2 1.50 m from top, submerged exposure		
	Point 1	Point 2	Point 3	Point 1	Point 2	Point 3
Oct 2010	0.23	0.18	0.24	0.26	0.22	0.31
Apr 2012	0.35	0.28	0.32	0.33	0.38	0.40

water level, see Fig. 1. While the average tide is only 0.10 m, normal water level variations due to wind are ±1.10 m, and extreme variations are ±2.00 m [17]; see Fig. 2.

2.3. Investigations

After nine years of exposure, the panel was lifted out of the seawater and cleaned using a high-pressure washer to remove any sea life from the surface. Subsequently, the panel was wrapped in plastic and transported to the Danish Technological Institute, where six cores (Series 1) were drilled. Before further investigation, these cores were wrapped in plastic and stored at room temperature. After coring, the panel was again wrapped in plastic and transported to the Chalmers University of

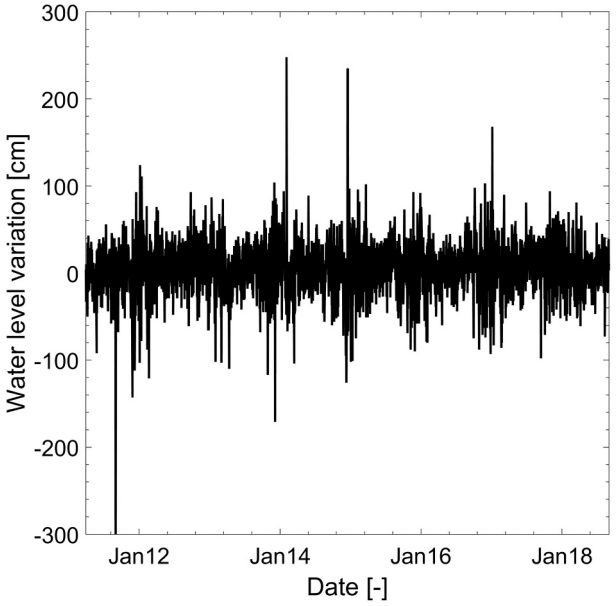

Fig. 2. Water level variation from January 2012 to January 2018. Zero (0) corresponds to the mean water level [9].

Table 4
Overview of investigations undertaken. The reinforcing bars are numbered from the right (facing the cracked surface). Information on the location of cores, exposure, and reinforcement type, is given in Fig. 1.

		Cores Series 1						Panel	
		C1	C2	C3	C4	C5	C6	Cores Series 2	Panel in general
Exposure	Tidal	X	X	X					
	Submerged				X	X	X		
Reinforcement	Conventional			X			X		
	Instrumented	X	X		X	X			
Crack morphology	Visual inspection	X			X			X	
	μ-CT	X	X	X	X	X	X		
	μ-XRF	X			X				
	Petrography		X			X			
Composition	μ-XRF	X			X				
	Petrography								
	Carbonation test	X			X				
	Chloride test								X
Corrosion state	Visual inspection	X	X	X	X	X	X	X	X

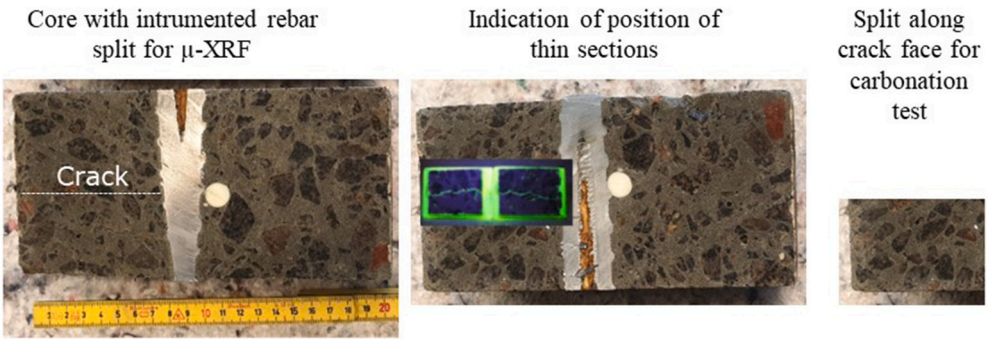

Fig. 3. Schematic illustration of sub-sectioning of cores from Series 1. Exposed surface to the left. Full length of cores (thickness of panel) 200 mm.

Table 5
Information obtained by the techniques applied for crack morphology characterization in the present study.

Technique	Resolution	Dimensions	Open crack	Entire crack	Self-healing products
μ-CT	116 μm/pixel	3D	X	–	–
μ-XRF	80 μm	2D	X	X	X
Petrography	1 μm[a]	2D	X	X	X

[a] Fluorescent light; 200× magnification.

Technology in Gothenburg, Sweden.

Table 4 summarizes the investigations undertaken, and Fig. 3 illustrates the sub-sectioning of cores from Series 1 for the μ-XRF analysis (shortened to μ-XRF in the remaining text) and carbonation test of the crack face as well as the positions of the thin sections. The six Series 1 cores (ø100 mm) were drilled in cracked areas of the three middle bars (one conventional and two instrumented) for detailed crack morphology and composition analysis using visual inspection, μ-CT, μ-XRF, and petrography. At Chalmers, the panel was visually investigated, additional cores (Series 2) were extracted, and the remaining reinforcement was excavated to identify any corrosion there might be. Table 5 summarizes the Information obtained from the techniques applied for crack morphology characterization in the present study. Note that cracks near the rebar could not be (entirely) detected (or therefore quantified) by μ-CT due to a combination of low resolution and image noise, artefacts associated with the scanning, see Fig. 4.

2.3.1. Investigation of Series 1 cores

2.3.1.1. Visual inspection. A standard crack-width ruler was used to determine crack widths on the cylindrical surfaces of the two cores (C1 and C4), subsequently investigated using μ-XRF.

2.3.1.2. X-ray micro-computed tomography (μ-CT). X-ray micro-computed tomography (μ-CT) was undertaken to characterize crack morphology on all six cores (C1–C6). The μ-CT was performed at the 3D Imaging centre at DTU using an 'XT H 225 ST' scanner from Nikon Metrology. Each core was investigated with three overlapping CT scans to cover the full height of the core. The μ-CT system was set up with the X-ray source in reflection geometry, and all scans were made with 200 kV high voltage and 75 W power and using 1 mm of tin as a filter between the source and the specimen. Given the cone-beam geometry, the efficient pixel size was 116.64 μm. The detector was binned to a size of 1024 times 1024 pixels. Each projection image consists of four frames, and projections were acquired over 360 degrees in 1571 steps, each with an exposure time of 1 s resulting in 1571 projection images. Each data set was reconstructed to a 3D volume using the Nikon Metrology software 'CT Pro 3D version 3.1.5098.29005', which is based on an FDK implementation of a filtered back-projection algorithm [18]. Segmentation and image analysis was undertaken is described below in Section 2.4.

2.3.1.3. Petrography. Petrography was undertaken on two instrumented reinforcing bars (C2 and C5). Two thin sections were prepared from each core, i.e., C2 and C5, to cover almost the entire crack length from the exposed surface to the reinforcement. The cores were cut transversal to the crack plane (see Fig. 3) using a rock saw and limited amounts of cooling water. The relevant concrete pieces were impregnated with fluorescent epoxy before lapping and thin section preparation. The thin sections were investigated using optical polarizing microscopy including a fluorescent light mode to characterize the extent of leaching and carbonation inside the crack, quantify the changes in

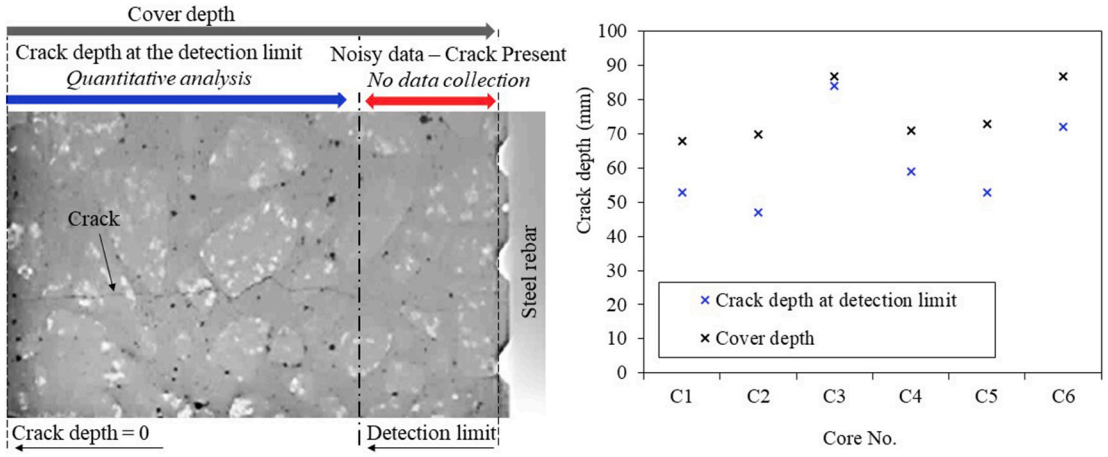

Fig. 4. Schematic illustration of detection limit for quantitative analysis of μ-CT scans due to low resolution and image noise, artefacts associated with scanning near rebars. Left: a representative crack with identification of limit for image segmentation. Right: the crack depths at the detection limit and the cover depth for all six cores (Series 1) investigated.

porosity, describe the mechanical damage, and characterize secondary phases formed in the crack.

2.3.1.4. Micro X-ray fluorescence spectrometry (μ-XRF). Micro X-ray fluorescence spectrometry (μ-XRF) mapping was undertaken on cores C1 and C4 using the scanner at the Department of Structural Engineering, NTNU in Trondheim, to determine the elemental content of chlorine and other selected elements in the cement paste. Shortly before the scanning, the cores were cut transversal to the crack planes (see Fig. 3) using a rock saw and limited amounts of cooling water. The μ-XRF elemental mapping of the concrete was performed with an M4 Tornado instrument from Bruker. The settings for data collection were 50 kV accelerating voltage, 600 μA current, spot size 20 μm, 80 μm distance between each pixel, 2 ms/pixel acquisition time, and 20 mbar vacuum atmosphere. It should be noted that the scans are not directly comparable because no reference samples were used to calibrate the measurements.

2.3.1.5. Carbonation detection. The carbonation depth was detected in the non-cracked bulk concrete and along the crack plane (see Fig. 3) on cores C1 and C4 using a rainbow indicator.

2.3.1.6. Inspection for reinforcement corrosion. Reinforcement corrosion was assessed visually on cores C1–C6 by inspecting the steel surface and the reinforcement imprint in the concrete. The reinforcement was removed carefully from the concrete with a hammer and chisel (cores C2 and C4) or using a saw for cutting wedges and then hammer and chisel (cores C1, C3 and C5–C6). Subsequently, the pieces of instrumented rebars were split longitudinally for internal inspection.

2.3.2. Investigations on panel and Series 2 cores

2.3.2.1. Visual inspection of panels and crack pattern characterization. Upon arrival at Chalmers, the panels were visually inspected, and the crack patterns were characterized. To allow for a detailed investigation of the crack morphology, ø100 mm cores (Series 2) were extracted from each location of cracks crossing reinforcement (i.e., rebar #1, #2, #6, and #7 in both the tidal and submerged zones). The drilling was undertaken at minimum speed to limit further mechanical damage. The surface crack width is an average of four measurements taken at a 20 mm distance in the cored areas. An electronic microscope was used on the panel surface, and the pictures were scaled against 1 mm. A mechanical microscope was used on the cylindrical surfaces of cores,

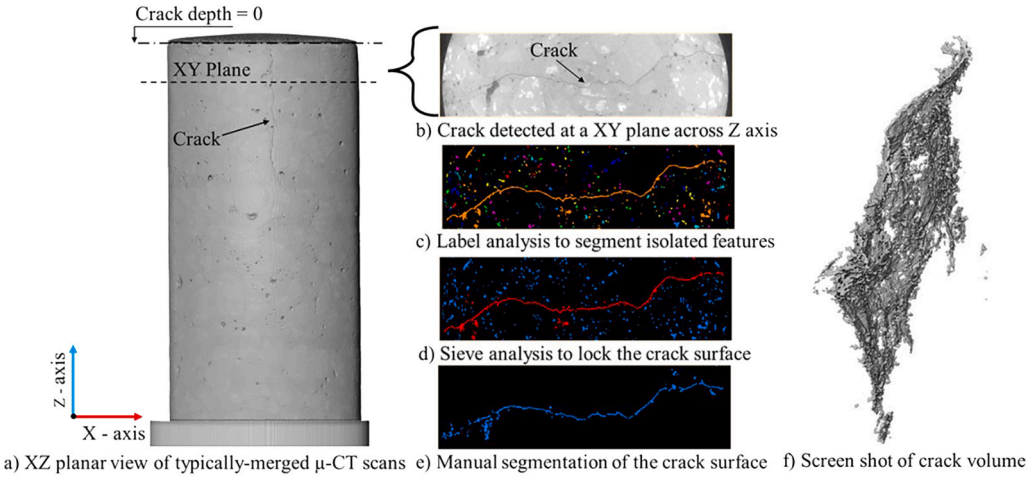

Fig. 5. Schematic illustration of a) an XZ planar view of typically-merged μ-CT scans, b)–e) the process followed to segment the crack in 3D space using the relevant modules available in Avizo, and f) a representative screenshot of the 3D crack volume illustrating the crack from a specific angle. Images of core C1.

and crack widths were measured every 20 mm. The estimate error is ±0.05 mm when using either an electronic or a mechanical microscope.

2.3.2.2. Chloride ingress detection. A colorimetric test for free chlorides was undertaken on split cores (Series 2 cores from rebars #1, #2, #6, and #7). The cores were split along the crack using a wedge and a hammer and sprayed with silver nitrate (0.1 N $AgNO_3$, corresponding to approx. 0.1 % of concrete [19]).

2.3.2.3. Inspection for reinforcement corrosion. The remaining rebars were removed using a rock saw, cutting vertically at approximately 1 cm from the rebars and using a small hammer and chisel to remove the remaining concrete. The rebars were then cleaned by sandblasting, and then the extent of corrosion was determined by visual inspection.

2.4. Crack segmentation from μ-CT scans

The μ-CT data acquired for the six cores from Series 1 (C1–C6) were analysed to characterize the qualitative and quantitative crack morphology. Data visualization and image analysis software Avizo was employed to perform the μ-CT data analysis. Vertical stitching was conducted during scanning to envelop the entire core volume within the available field of view, producing three different stacks of images per core. These three different datasets per core were initially converted from 32-bit to 16-bit using ImageJ to minimize computational cost and were then merged using image registration techniques to create and visualize the entire core volume, as shown in Fig. 5. A consistent methodology was conceived and applied to all samples to enable comparison. Intensity thresholding was performed primarily to segment the voids from concrete aggregate and hardened cement paste in characteristic 2D XY planar ortho-slices. Pores and cracks, both included in the voids phase, have identical values in the corresponding intensity histogram, requiring additional processing to enable crack isolation. Label analysis followed by sieve analysis – both modules available in the Avizo image segmentation toolset – separated the crack from the pore network. Final polishing of the crack volume was performed by employing "brushing" tools – a user-defined approach available in Avizo.

The methodology applied is illustrated in Fig. 5 across a 3D profile of a representative crack and was implemented for all samples investigated. The selection of appropriate intensity thresholding range was consistent on all occasions to facilitate comparison. Image segmentation employed to separate cracks failed to provide quantitative data at crack depths near the rebar due to noise artefacts present in the corresponding image datasets induced by the steel rebar. Data were therefore, collected from zero crack depth to the image segmentation detection limit (see Fig. 3). It should be noted that visual observation of μ-CT images near the steel rebar confirmed that the cracks had fully penetrated the concrete cover.

The following metrics were selected for crack characterization:

- Crack area: the area of a crack in a given XY plane; the XY-planar crack area used describes the crack at a given depth (see Fig. 5a); (mm^2).
- Effective crack length: the actual length of the crack (mm), measured using a digital ruler available in the Avizo toolset; (mm).
- Nominal crack length: the length of the secant between the two points of the crack where the exposed surface and the cylindrical surface meet; (mm).
- Equivalent crack width: the crack area at a specific crack depth divided by the corresponding effective crack length. No errors were calculated; (mm).
- Measured mean crack width: an alternative methodology to derive crack width using the digital ruler available in the Avizo toolset. The digital ruler was used to measure the crack width at 10 locations across the crack (XY plane) at given crack depths. A mean value was recorded, and the standard deviation was calculated; (mm).
- Crack tortuosity: the ratio between the effective crack length and the nominal crack length in a given XY plane; (−).

Since the cracks formed at distinct locations within the sample's volume, normalization is required to achieve a valid comparison between the cores. Two different methodologies were applied. The first method was based on the XY planar crack area, known at every crack depth down to the detection limit. Representative 2D XY plane projections were selected across the crack depth (i.e., Fig. 4b), and the corresponding effective crack length was measured. The ratio between the XY planar crack area and effective crack length, i.e., the equivalent crack width, was determined at specific crack depths. The second methodology included direct measurements of crack width across the effective crack length at different crack depths. A mean value (mean crack width) was calculated at each crack depth. Only a proportion of 2D XY projections was used for calculations.

Crack tortuosity was also calculated from the acquired tomographic datasets. Using the available toolset for digital measurements, the effective crack length was determined in distinct sample XY planar positions. The nominal crack length was also measured in the same planes. Tortuosity was calculated as the ratio of effective crack length to nominal crack length.

3. Results

3.1. Visual appearance of panels

Seashells were found attached to the submerged part of the panel when it was extracted from the exposure site, but apart from traces of biological growth, the panel appeared undamaged after cleaning.

3.2. Crack morphology

3.2.1. Visual determination

The cracks were in general visible, but the crack width was difficult to measure using the naked eye. Visually determined crack morphology (aided by an electronic/mechanical microscope) on the panel, the Series 2 cores, and the Series 1 cores C1 (tidal exposure) and C4 (submerged exposure) are summarized in Table 6 and Table 7, respectively. While the surface crack widths given in Table 6 were determined on the exposed panel surface, the numbers given in Table 7 were determined on the cylindrical surfaces of the two cores (C1 and C4) which were subsequently split (see Fig. 3) and investigated using μ-XRF.

3.2.2. Petrography

Fig. 6 shows impregnated pieces cut off after thin sectioning prepared from cores from the tidal (C2) and submerged (C5) exposure zones of the panel. Open cracks are observed to reach the reinforcement level in both cores.

One crack is seen in core C2 from the surface of the concrete to the imprint of the rebar. The crack traverses aggregate and occasionally splits into smaller cracks. The main crack has a width of 60–80 μm at the surface and narrows to 15 μm at the rebar. The cracks are generally open, but the main crack is bridged by calcite for the last 0.2 mm up to the surface.

The initially introduced crack in core C5 is seen from the surface of the concrete to the imprint of the rebar. An empty crack, possibly formed when the rebar was removed from the concrete, has been generated along this crack. The initial crack traverses aggregate and occasionally splits into smaller brittle cracks. The main crack has a width of 200 μm at the surface and narrows to 13 μm at the rebar. The initial cracks are generally open, but the main crack is bridged by calcite for the last 3 mm up to the surface.

Table 6
Crack morphology after nine years of exposure determined on panel (using electronic microscope; ±0.05 mm) and Series 2 cores (using mechanical microscope; ±0.05 mm).

Location, bar #	Crack 1 tidal exposure				Crack 2 submerged exposure			
	1	2	6	7	1	2	6	7
Surface crack width (mm)	0.32	0.28	0.11	0.36	0.10	0.10	0.20	0.03
Crack depth (mm)	100	120	100	80–130	100	120	80	60–80
Crack width at rebar/max depth (mm)	0.10	0.30	0.02	0.05	0.15	0.20	0.04	0.14
Average crack width (mm)	0.47	0.30	0.18	0.18	0.15	0.20	0.04	0.15
Standard deviation, crack width (mm)	0.34	0.20	0.20	0.14	0.06	0.12	0.38	0.21
Free chloride detected at rebar	Yes	Yes	–	No	Yes	No	–	No

Table 7
Visually determined crack morphology on cylindrical surfaces of cores C1 (tidal exposure) and C4 (submerged exposure) from Series 1 using a common crack-width ruler. Positions A and B indicate the two positions on the cylindrical surface where the crack can be observed.

Core		Position A	Position B
C1	Visible crack depth mm)	175	135
	White precipitate	Localized, up to a depth of 60 mm	Localized, up to a depth of 100 mm
	Crack width (mm)	0–20 mm depth: ≤0.8 20–40 mm depth: 0.20–0.25	0–20 mm depth: <0.5 20–30 mm depth: <0.2 90–100 mm depth: <0.2
C4	Visible crack depth (mm)	110	100
	White precipitate	Localized, up to a depth of 100 mm	Localized, up to a depth of 75 mm
	Crack width (mm)	0–8 mm depth: <1 15–45 mm depth: 0.2–0.3 >45 mm depth: ≤0.1/ uncertain	0–35 mm depth: <1 35 mm depth: 0.15 >35 mm depth: ≤0.1/ uncertain

3.2.3. μ-CT

All the cracks were positioned almost perpendicular to the exposed surface, and visual observation of μ-CT images near the steel rebar confirmed that the cracks had fully penetrated the concrete cover. However, due to the detection limit, the cracks could not be quantified in the vicinity of the rebars (see Fig. 4). The quantification given below therefore only covers part of the cracks. As supplementary material, crack volume 3D profiles are also given.--

The distribution of XY planar crack area across the crack depth is given in Fig. 7 for all six cores of Series 1. The results indicate fluctuations for all cores, among which C5 showed the lowest maximum crack area. A common trend is observed from the exposed surface to the greatest depths for all cores investigated:

- The crack in the top part of the cores (~0–10 mm crack depth) exhibits an initial increase in the XY planar crack area (i.e., the crack widens) from the exposed surface and down.
- The trend of growing crack area with crack depth reverses at depths beyond approximately 10 mm.
- The crack is narrow (or below the detection limit) in the vicinity of the rebar (large crack depths). This behaviour is generally to be anticipated since the cracks were initially introduced due to bending in the concrete slab.

The cores could not be compared based on the XY planar crack area since the crack locations differ among the cores. As explained in Section 2.4, therefore, two different methodologies were adopted to compare the cores: a) the equivalent crack width, and b) the measured mean crack width.

The measured mean crack width method is strictly user-defined since manual measurements were made. The available resolution, which was considerably limited because the entire sample thickness had to be probed, affected the reliability of the high-sensitivity crack width measurements (typical crack width ~ 2–3 pixels). Corresponding error bars have been included to take account of the potential variation in the measurements performed.

The results enable a comparison of the crack geometry between all six cores investigated, cancelling the effect of crack location in the core. Except for core C2, an increase in equivalent crack width is observed during the transition from the exposed surface down to 10 mm of crack depth, which agrees with the results shown in Fig. 7. While fluctuations are also present, a general trend of decreasing crack width values is observed beyond 10 mm crack depth. Fig. 8 compares the two different methodologies adopted. Good agreement can be observed, considering the limitations related to the resolution.

Finally, crack tortuosity was also investigated using the available μ-CT image dataset. Representative 2D XY plane projections (five per core) were used to calculate the effective and the nominal crack length (Section 2.4) in the XY plane. The results are illustrated in Fig. 9. Numbers close to 1.00 might be explained by self-healing, closing part of the crack and reducing the effective crack length.

3.3. Precipitation in cracks

3.3.1. Visual inspection

Localized white precipitation was observed to depths of 100 mm in both visually inspected cores from Series 1, i.e., C1 (tidal) and C4 (submerged); see Table 7. The chemical composition of the white precipitate was not directly characterized, but μ-XRF mappings on the cut surface gave an indication of magnesium and calcium-rich phases inside in the crack. The type of white precipitate observed is typical for cracked concrete in a marine environment. The white precipitate usually contains brucite ($Mg(OH)_2$) and calcite ($CaCO_3$), but precipitation of ettringite ($Ca_6Al_2(SO_4)_3(OH)_{12}{\cdot}26H_2O$) has also been observed [20]. Precipitation of magnesium has been observed as far as 100 mm from the exposed surface inside a crack after 50 years of marine exposure [21].

3.3.2. Petrography

The petrographic investigations indicate that the cracks are still open, as seen in fluorescent light mode (Fig. 6), but various deposits are seen on the crack faces and in the crack. These deposits were identical in the two tidal (C2) and submerged (C5) exposed cores and were as follows from the exposed surface and inwards in the crack: calcite, followed by brucite, and deeper inside the cracks, first portlandite (calcium hydroxide, $Ca(OH)_2$) and then ettringite. These observations are similar to observations made on cores from the cracked beams of three different types of infrastructure concrete after 25 years of marine exposure [20]. Table 8 summarizes the findings from the petrographic study and shows the depths from the surface to which the deposits were observed. The petrographic study also showed shallow and uneven carbonation of the outer exposed surfaces (C2: 0–1.2 mm, C5: 0–2 mm), as well as shallow carbonation along the crack faces at greater depths from the exposed surfaces (C2: 0.8–20 mm, C5: 3–8 mm) and carbonation in part of the

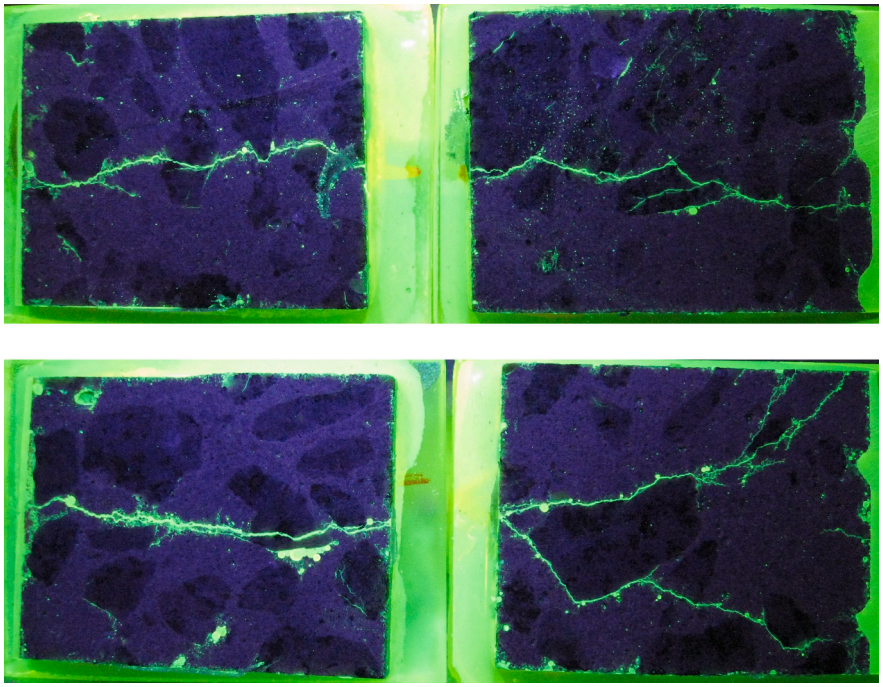

Fig. 6. Fluorescent impregnated thin sections (two per core) showing impregnated (green) cracks in cores C2 (tidal exposure) and C5 (submerged). The exposed surface is to the left in the left-hand thin sections, and the imprint after the rebar is to the right in right-hand thin sections. The dimensions of the fluorescent impregnated pieces cut off from the thin sections are $30 \times 45\ mm^2$.

Table 8
Microstructural features (deposit/mineral phases found in the cracks) determined by petrography on thin sections from cores C2 (tidal exposure) and C5 (submerged exposure).

Core	Depth (mm)	Deposit/mineral phases found in the cracks
C2	0–0.2	Bridging with calcite at crack mouth, partially closing the crack
	0.2–0.8	Lining of crack faces with pure calcite
	0.8–3	Lining of crack faces with a mixture of calcite and brucite
	3–4	Lining of crack faces with mainly brucite
	4–22	Crack is mainly empty
	22 to rebar imprint	Rather large crystals of calcium hydroxide and ettringite are randomly precipitated in the crack to the position of the rebar
C5	0–3	Bridging with calcite at crack mouth, partially closing crack
	3–4	Lining of crack faces with a mixture of calcite and brucite
	4–20	Crack is mainly empty, but difficult to observe due to the later cracking
	20–22	Large calcium hydroxide crystals are observed in the crack
	22–25	Crack almost filled and closed with calcite
	25 to rebar imprint	Rather large crystals of calcium hydroxide are randomly precipitated in the crack

rebar imprint in the submerged core (C5). Finally, the paste appeared fully de-calcified with increased porosity in the outer exposed surfaces to depths of 7 mm in C2 and 5 mm in C5.

3.3.3. μ-XRF

Mg was visible within the first 10 mm of the cracks in both cores (C1 and C4) investigated using μ-XRF (see Appendix 1).

3.4. Composition of concrete

3.4.1. Free chloride content

Free chlorides were observed in some but not all places at the steel–concrete interface in the vicinity of the transversal crack and were affected by slip and separation (see Table 6).

3.4.2. Carbonation

At the cut surface, the concrete did not show visual/macroscopic signs of carbonation (Fig. 10, left), which is similar to the petrographic analysis showing only shallow (1–2 mm) carbonation. The concrete surface colour was violet to blue, indicating a pH between 11 and 13. However, a carbonation front of about 20–30 mm was detected when the concrete was split along the crack face. This is also in line with the observations made in the petrographic analysis that showed carbonation along the crack face to a depth of 20 mm for core C2 (tidal exposure). The colour of the concrete was green in the outer 20–30 mm, indicating a pH of around 9 (Fig. 10, right). Furthermore, the carbonation of the upper part of the crack face coincided with a white precipitate. The carbonation depth appeared deeper along the cylindrical outer surface of the core (Fig. 10, right), suggesting carbonation during storage (approximately six weeks wrapped in plastic and stored at 5 °C). However, this is not in agreement with the lack of/limited carbonation on the exposed surface (Fig. 10, left), so it is assumed to be an artefact. Note that the petrographic analysis showed less carbonation along the crack face (to a depth of 8 mm) for the submerged exposed core (C5) than for the core from tidal exposure (C2). The petrographic analysis also showed shallow carbonation of part of the rebar imprint in core C5 (submerged exposure), which was not observed in the visual/macroscopic investigation. Similar observations were made for core C1 (tidal exposure) and C4 (submerged exposure).

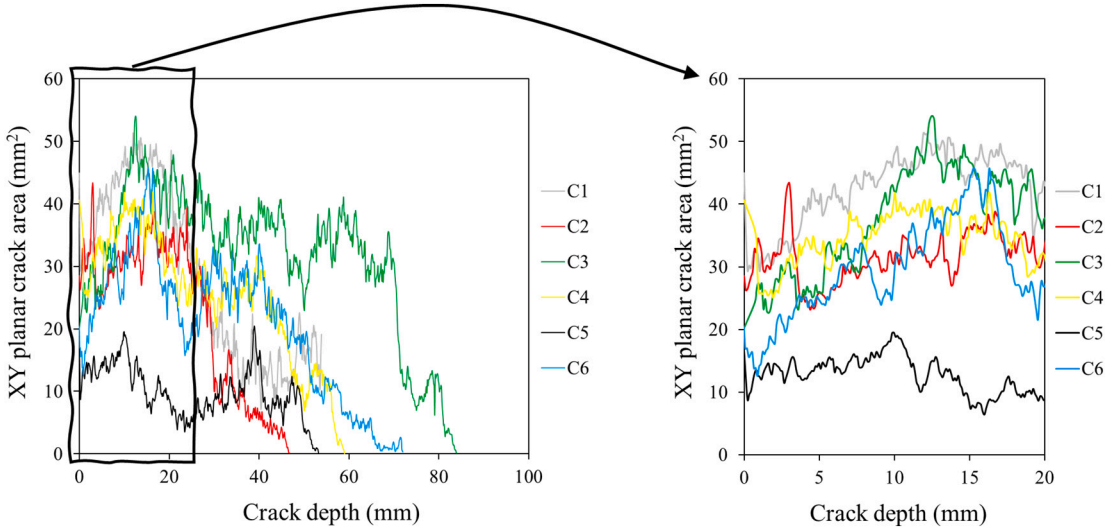

Fig. 7. Measured XY planar crack area distribution across the crack depth for each core investigated using μ-CT. (For interpretation of the references to colour in this figure legend , the reader is referred to the web version of this article.)

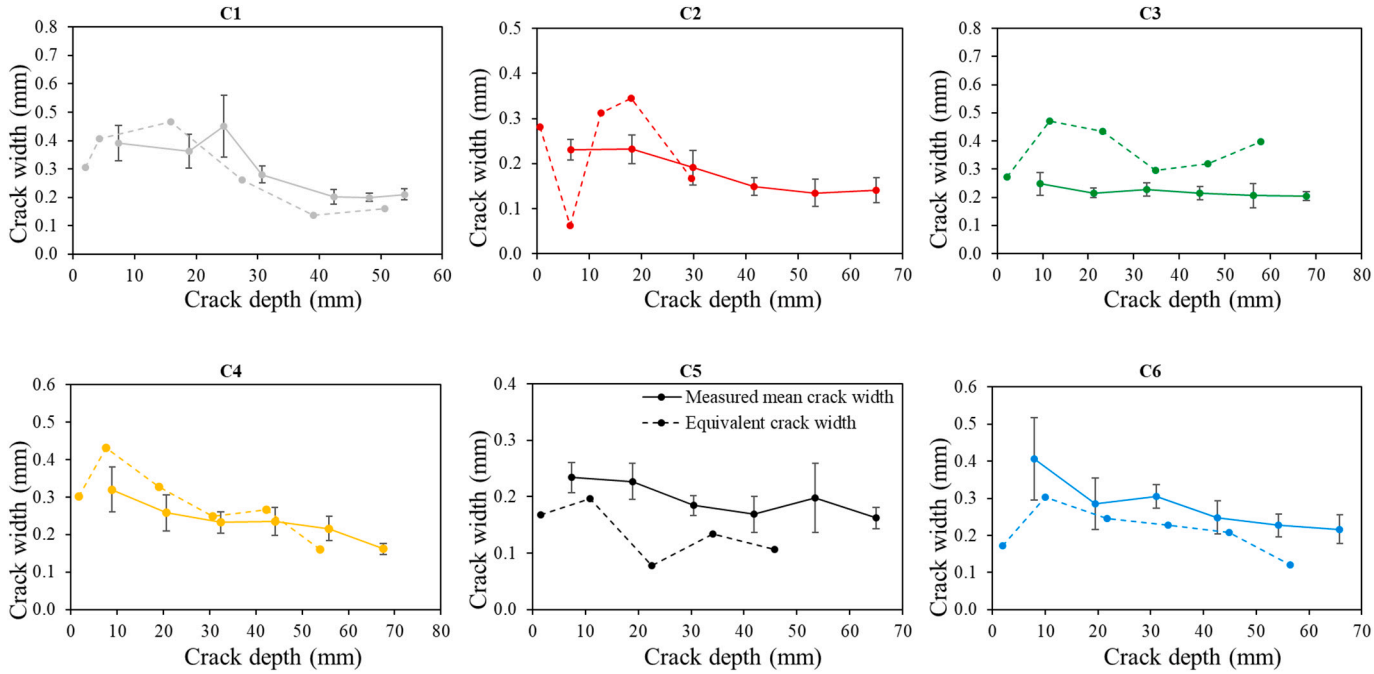

Fig. 8. Comparison between the two methodologies adopted to quantify crack widths from μ-CT scans.

3.4.3. Elemental mapping

Elemental maps for Ca, Si, Al, Na, K, Mg, Cl and S in cores C1 and C4 are shown in Appendix 1. Due to the experimental setup, the maximum width of a scan was 180 mm, and the cores were therefore not scanned at their full length (200 mm). Moreover, it should be noted that the intensities were normalized to the highest measured counts in each elemental map (each picture). Therefore, the same colours do not necessarily mean similar concentrations. Furthermore, that the apparently high sulphur content in part of the steel–concrete interface of core C1 is an artefact due to mechanical damage during sample preparation.

3.5. Corrosion state

3.5.1. Conventional reinforcing bars

When we investigated all the steel reinforcement in the panel (except the parts present in already extracted cores), none of the reinforcement bars showed significant signs of corrosion, irrespective of their proximity to cracks, and no corrosion pits were visible to the naked eye after sandblasting. The only corrosion observed was in a tying wire connecting a reinforcing bar to a spacer.

Neither was significant corrosion observed on the surface of the steel in the extracted cores. After the concrete cores were cut (for μ-XRF),

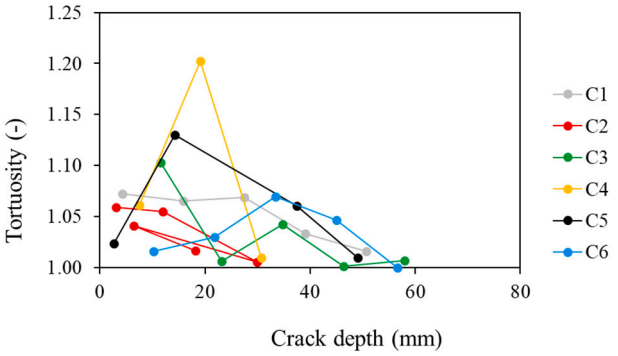

Fig. 9. Crack tortuosity distribution across crack depth for all six cores investigated using μ-CT. (For interpretation of the references to colour in this figure legend , the reader is referred to the web version of this article.)

there were no indications of corrosion at the rebar–concrete interface. The bond between rebar and concrete appeared good, and the reinforcement condition generally appeared very good. One minor corrosion spot was found on the reinforcement of core C1 close to the crack (Fig. 11). The corrosion spot appeared only superficial and had a length of about 5 mm. Furthermore, a white precipitate was found on one side of the reinforcement surface in core C1 (Fig. 11, right).

3.5.2. *Instrumented reinforcing bars*

We found that 7 out of 20 pins embedded in the instrumented rebars investigated at Chalmers were no longer electrically disconnected from each other. Furthermore, crevice corrosion was consistently found in all the extracted pins. Similar observations were made for the instrumented rebars present in cores C1 and C2 (Series 1), for which a large amount of corrosion products was found inside the hollowed bars.

4. Discussion

This study aimed to investigate further the impact of cracks on the corrosion of conventional steel reinforcement in marine-exposed cracked concrete and to explain the observed monitoring data. The panel investigated was instrumented, and monitoring data from more than five years of exposure indicated reinforcement corrosion measured on instrumented rebars positioned at a depth of approximately 85 mm and crossed by bending cracks [9]. The apparent active corrosion appeared at unexplained cyclic intervals and called for the present investigation. A central part of the study was the characterization of the crack morphology and the corrosion stage of the reinforcement because most of the current literature indicates rapid corrosion initiation in the presence of cracks. This section therefore starts with a short discussion on the applicability of the applied methods for the characterization of crack morphology before discussing the state of the reinforced concrete panel after nine years of marine exposure.

Besides visual inspection, three techniques were used to characterize the crack morphology: μ-CT, μ-XRF, and petrography. None of these techniques can provide all the required information by itself, but detailed information on the crack morphology, ingress and possible phase changes can be derived from a combination of the various techniques. When comparing the obtained data, it should be noted that besides providing different information, the methods were applied at different locations of the panel.

Destructive techniques, such as μ-XRF, petrography, and extraction of material for visual inspection require sample preparation, including cutting plane surfaces and preparing fluorescent-impregnated thin sections, while also providing 2D information on the elemental mapping, crack morphology, phase changes, and corrosion stage of the reinforcement. Non-destructive μ-CT, on the other hand, provides a 3D image of the core and crack, but low resolution and image noise artefacts associated with the scanning hamper the detection and quantification of cracks near the reinforcement. Moreover, while μ-CT provides a characterization of the open crack, both μ-XRF and petrography provide information on the original crack, the open crack, and possible self-healing products.

Fig. 12 gives a comparison between results obtained from μ-CT and petrography data for cores C2 (tidal exposure) and C5 (submerged exposure).

4.1. *Crack morphology and self-healing*

Both CT scans and impregnated thin sections illustrate the crack morphology. The impregnated thin sections show that open cracks penetrate the entire cover and reach the steel reinforcement (Fig. 6). Similar observations were made on the CT scans, but due to low resolution and image noise artefacts associated with the scanning, the crack morphology could not be quantified in the vicinity of the rebars based on the CT images. The cracks appear finer in the 10–20 mm closest to the reinforcing bars, which is in line with the CT scans.

The two cracks were produced using three-point bending and were therefore expected to be tapered (V-shaped). The surface crack width was initially 0.22–0.31 mm (Table 3). After nine years of exposure, the surface crack widths measured on the panel were, on average, 0.27 mm (range 0.11–0.36 mm) in the tidal zone and 0.11 mm (range 0.03–0.20 mm) in the submerged zone (Table 6). This difference may be due to possible self-healing in the near-surface region of the crack in the submerged exposure [20]. If there were no self-healing, we would expect a tapered crack with the largest crack width at the exposed

Fig. 10. Carbonation detection on core C1. Left: freshly cut concrete core sprayed with rainbow indicator; Right: crack face sprayed with a rainbow indicator (left side: cut surface; right side: outer cylinder surface). (For interpretation of the references to colour in this figure legend , the reader is referred to the web version of this article.)

Fig. 11. Minor corrosion spot detected in C1; Red circle: Spot on reinforcement bar; Red arrow: Spot in the concrete imprint; Crack marked in white. (For interpretation of the references to colour in this figure legend, the reader is referred to the web version of this article.)

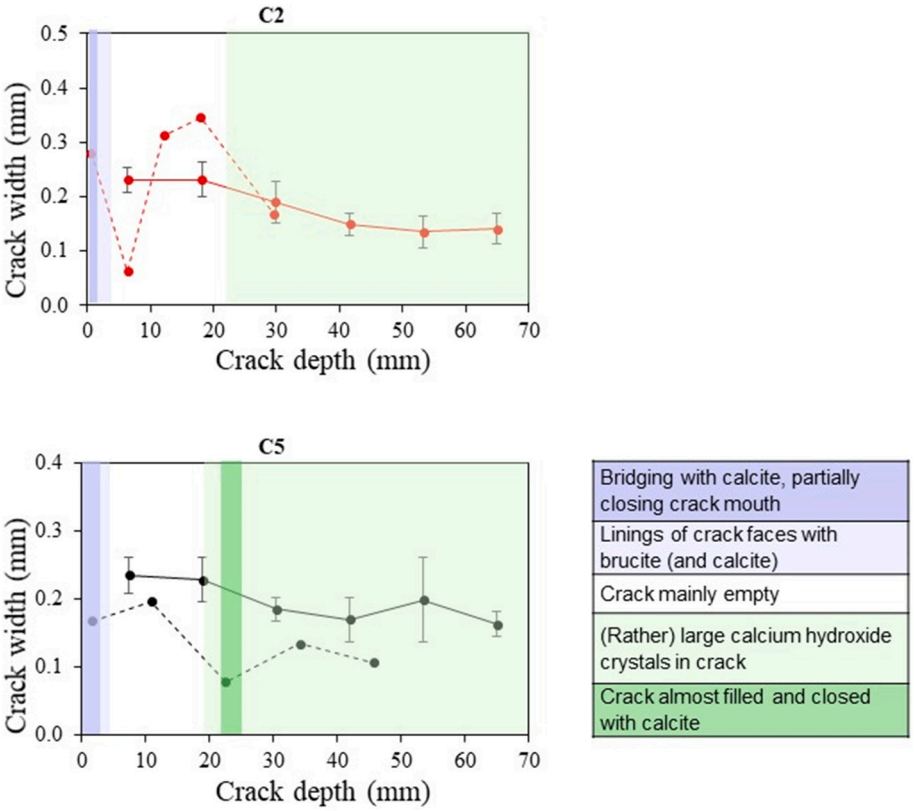

Fig. 12. Comparison of crack characterization using μ-CT (equivalent crack width (dotted line) and measured mean crack width (solid line), data from Fig. 8) and zones identified using petrography (data from Table 8) for cores C2 (tidal exposure) and C5 (submerged exposure). (For interpretation of the references to colour in this figure legend, the reader is referred to the web version of this article.)

surface. After nine years of submerged marine exposure, the observation a of reduced crack area can be explained by the precipitation of calcite, brucite and portlandite crystals, partly closing the crack near the exposed surface. If we generalize the findings from this study and consider a vertical surface, it should be noted that horizontal cracks (as in this study) are expected to have a greater ability to self-heal than vertical cracks [21].

We observed more variation between cores in the same exposure zone than in the detected crack area using μ-CT, but also, as expected, the greatest crack area was observed in a core from the tidal exposed part of the panel (C3) and the smallest crack area was observed in a core from the submerged part of the panel (C5).

4.2. Ingress and elemental changes

The petrographic study showed that the first 5 mm of the paste was fully de-calcified with increased porosity in the tidal and submerged zones. If the elemental maps of Mg, S and Cl obtained by μ-XRF (Fig. 13)

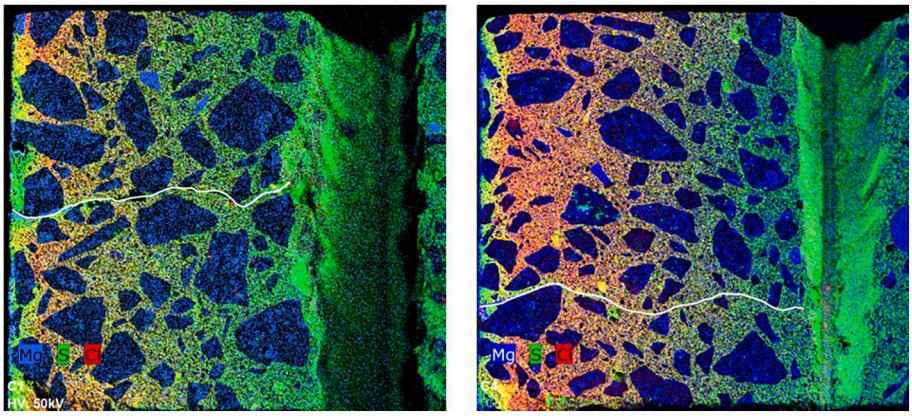

Fig. 13. Elemental zonation of Mg (blue), S (yellow) and Cl (red) in core C1 (left) and C4 (right). Cracked and exposed surfaces of panels to the left and imprints of rebars to the right in both figures. Mg is visible within the first 10 mm of the crack. Note that the apparent high S content in part of the steel–concrete interface of core CI is an artefact due to mechanical damage during sample preparation. (For interpretation of the references to colour in this figure legend, the reader is referred to the web version of this article.)

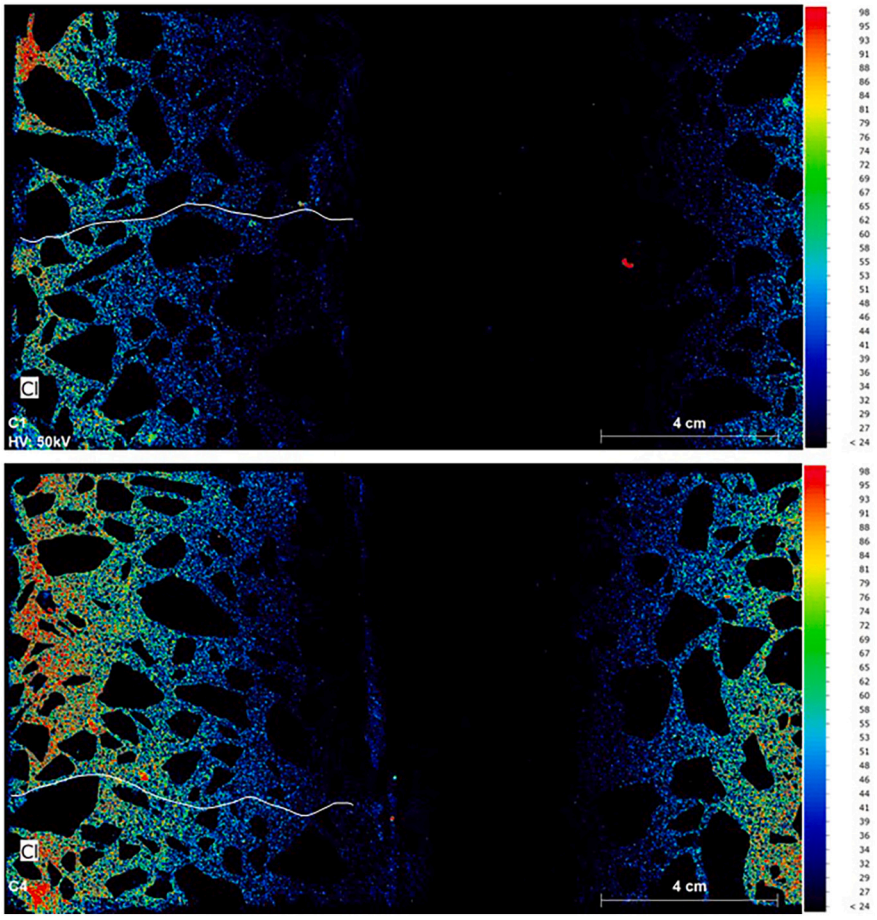

Fig. 14. Map visualizing chloride ingress depth in relative intensities: core C1 (tidal exposure) at the top and core C4 (submerged) at the bottom. The cracked surface of the panel is to the left. Cracks are marked in white. (For interpretation of the references to colour in this figure legend, the reader is referred to the web version of this article.)

are combined, a clear elemental zonation as reported by Jakobsen et al. [22] can be observed, with a thin Mg-rich surface layer, followed by a layer of about 0.5 cm enriched in S, followed by Cl. Fig. 13 shows that precipitation of Mg-rich phases was detected within the first 10–15 mm in both cracks. This is in line with observations reported of cracked concrete beams after 25 years of marine exposure in northern Norway [20].

The chloride ingress in core C1 (tidal exposure) and core C4 (submerged exposure) is shown in Fig. 14 with relative intensities. The intensities are normalized to the highest measured counts in each elemental map (each picture). This means that the same colours do not necessarily mean similar concentrations. As no calibration samples were available, it is impossible to draw any quantitative conclusions from the measurements. However, quantitative chloride profiles are available for a companion non-instrumented concrete panel after ten years at the same field station showing comparable ingress in tidal and submerged exposure [23].

Fig. 13 shows how the elemental zonation of Mg, S and Cl is also

observed around the crack within the first few centimetres, especially in core C4 (submerged exposure). Fig. 14 shows the chloride ingress maps, in which chlorides appear equally distributed over the whole width of the concrete cores except near the crack, where a slightly deeper ingress can be observed. Furthermore, chlorides have accumulated in detectable amounts along the reinforcement in the vicinity of the cracks. This is in line with other investigations that indicate that bending cracking initiates some damage (slip and separation) along the reinforcement, which then allows for faster ingress [10].

If we generalize the findings from this study, it should be noted that horizontal cracks on a vertical surface (as in this study) are expected to experience less chloride ingress than vertical cracks on a vertical surface and cracks on upward-facing horizontal surfaces [21].

4.3. Corrosion

The present data cover seven 1.80 m long reinforcing bars embedded in good quality concrete (w/b = 0.40 and cover >75 mm), each crossed by two cracks (surface crack widths 0.20–0.30 mm) with 0.80 m distance, one crack exposed in the tidal zone, one located in the submerged zone. The investigation showed no significant corrosion on the surface of the reinforcing bars in cracked or uncracked areas. Two of the seven reinforcing bars passed by the transversal cracks were instrumented bars. The apparent periodical corrosion activity identified by monitoring open circuit potentials during the first seven years of exposure [9] can be explained by extensive corrosion inside the instrumented reinforcing bars and on the interior of the pins. This corrosion is expected to be due to unintended ingress along cables and shows that the design of the instrumented reinforcing bars needs to be adjusted if used for long-term monitoring. Potential anodic protection could explain the lack of corrosion spots on the surface in contact with the concrete. However, with no other weaknesses, the remaining conventional rebars showed no impact from the cracks.

The absence of corrosion might be explained by the combination of the crack type (tapered), the crack orientation and location (horizontal on a vertical surface) [21], the large cover and the binder composition (Portland cement) providing a sustained high hydroxyl ion concentration. The combined impact of chloride and hydroxyl ions on steel corrosion in cementitious materials has been recently demonstrated by Marcos-Meson et al. [24] for steel fibre-reinforced mortars. Using steel fibres and mortar with limited aggregate size limits the potential impacts of other characteristics of the steel–concrete interface [25]. The potential detrimental impact of through cracks facilitating leaching and sustained chloride ingress has been observed for similar cover and dense infrastructure concrete resulting in visible but limited corrosion after 17 years [26].

5. Conclusions

A pre-cracked concrete panel (w/c = 0.40) was exposed to seawater for nine years at a marine exposure site in Denmark. Two tapered cracks were present with an initial surface crack width of 0.20–0.30 mm. The cracks were horizontal; one crack was located in the tidal zone, the other in the submerged zone. The following observations were made

1. The fully submerged crack exhibited decreased crack width due to precipitation of calcite, brucite and calcium hydroxide from the exposed surface and inwards, causing partial self-healing.
2. The cracks were observed to facilitate chloride ingress, and chloride was detected at the steel–concrete interface.
3. Corrosion was not found on the reinforcing bars in any significant amounts. The absence of corrosion might be explained by the combination of the crack type location, the large cover, and the binder composition (Portland cement), providing a sustained high hydroxyl ion concentration.
4. Earlier monitoring of open-circuit potentials indicating cycles of active corrosion starting 1–2 years after exposure [9] might be explained by extensive corrosion in the interior of the corrosion sensors in the instrumented reinforcement. The design of the instrumented reinforcing bars needs therefore to be adjusted if used for long-term monitoring.

Supplementary data to this article can be found online at https://doi.org/10.1016/j.cemconres.2022.107070.

CRediT authorship contribution statement

Michel and Geiker developed the panel design. Michel, Lundgren, Robuschi and Geiker were equally involved in planning the forensic study and collecting literature. Experimental investigations were undertaken by Robuschi (investigation of panel and cores Series 2), Danner (μ-XRF), Gundlach (μ-CT) and Jakobsen (petrograhy). Analysis of μ-CT scans was undertaken by Paraskevoulakos. All authors contributed to relevant parts of the manuscript and commented on the final manuscript.

Declaration of competing interest

The authors declare that they have no known competing financial interests or personal relationships that could have appeared to influence the work reported in this paper.

Data availability

Data will be made available on request.

Acknowledgements

The authors gratefully acknowledge financial support from Femern Bælt A/S, Sund & Bælt Holding A/S, and the Danish Agency for Science, Technology and Innovation in connection with the establishment of the panels, and Femern Bælt A/S for access to the data. We also gratefully acknowledge the Swedish Transport Administration's financial support of work undertaken at Chalmers University of Technology.

Appendix 1

Elemental maps from micro-XRF analysis

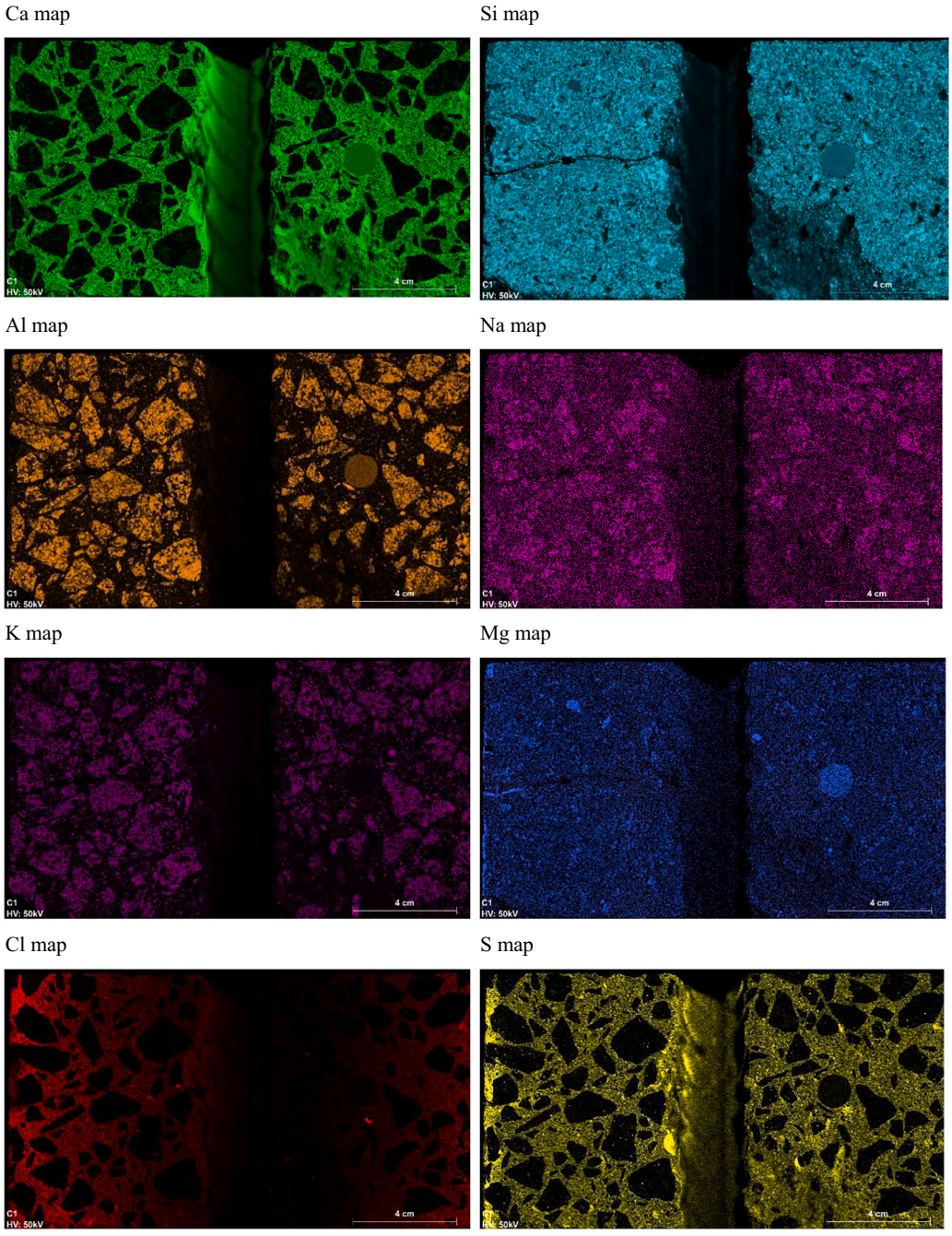

Fig. A1. Elemental overview maps of core C1, with the cracked surface of the panel to the left.

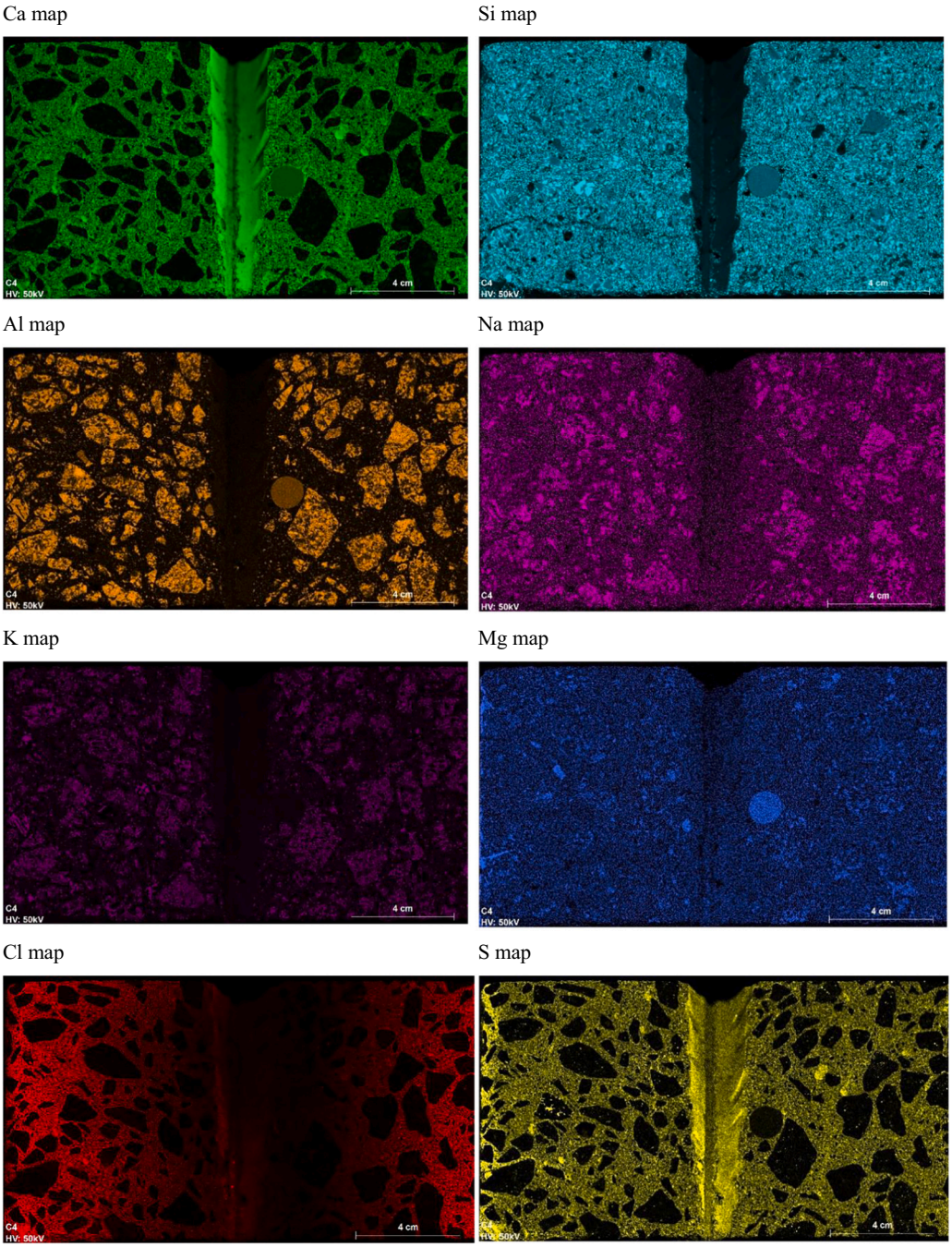

Fig. A2. Elemental overview maps of core C4, with the cracked surface of the panel to the left.

References

[1] B.J. Pease, Influence of Concrete Cracking on Ingress and Reinforcement Corrosion, PhD Thesis, Department of Civil Engineering, Technical University of Denmark, Lyngby, Denmark, 2010.

[2] A.C.B. Käthler, U.M. Angst, M. Wagner, C.K. Larsen, B. Elsener, Effect of cracks on chloride induced corrosion of steel in concrete – a review, in: Norwegian Public Roads Administration, NPRA Reports No. 454, Norwegian Public Roads Administration, Oslo, Norway, 2017.

[3] P. Schiessl, M. Raupach, Laboratory studies and calculations on the influence of crack width on chloride-induced corrosion of steel in concrete, ACI Mater. J. 94 (1997) 56–61, https://doi.org/10.14359/285.

[4] L. Yu, R. François, V.H. Dang, V. L'Hostis, R. Gagné, Development of chloride-induced corrosion in pre-cracked RC beams under sustained loading: effect of load-induced cracks, concrete cover, and exposure conditions, Cem. Concr. Res. 67 (2015) 246–258, https://doi.org/10.1016/j.cemconres.2014.10.007.

[5] A. Blagojevic, The Influence of Cracks on the Durability and Service Life of Reinforced Concrete Structures in Relation to Chloride-induced Corrosion: A Look From a Different Perspective, Delft University of Technology, 2016. PhD Thesis.

[6] K. Tammo, S. Thelandersson, Crack behavior near reinforcing bars in concrete structures, ACI Struct. J. 106 (2009) 259–267.

[7] K.G. Papakonstantinou, M. Shinozuka, Probabilistic model for steel corrosion in reinforced concrete structures of large dimensions considering crack effects, Eng. Struct. 57 (2013) 306–326, https://doi.org/10.1016/j.engstruct.2013.06.038.

[8] M. Geiker, T. Danner, A. Michel, A. Belda Revert, O. Linderoth, K. Hornbostel, 25 years of field exposure of pre-cracked concrete beams; combined impact of spacers and cracks on reinforcement corrosion, Constr. Build. Mater. 286 (2021), 122801, https://doi.org/10.1016/j.conbuildmat.2021.122801.

[9] A. Michel, H.E. Sørensen, M.R. Geiker, 5 years of in situ reinforcement corrosion monitoring in the splash and submerged zone of a cracked concrete element,

Constr. Build. Mater. 285 (2021), 122923, https://doi.org/10.1016/j.conbuildmat.2021.122923.
[10] A. Michel, A.O.S. Solgaard, B.J. Pease, M.R. Geiker, H. Stang, J.F. Olesen, Experimental investigation of the relation between damage at the concrete-steel interface and initiation of reinforcement corrosion in plain and fibre reinforced concrete, Corros. Sci. 77 (2013) 308–321, https://doi.org/10.1016/j.corsci.2013.08.019.
[11] A. Michel, V.M. Meson, H. Stang, M.R. Geiker, M. Lepech, Coupled mass transport, chemical, and mechanical modelling in cementitious materials: A dual-lattice approach, in: Life-Cycle Analysis and Assessment in Civil Engineering: Towards an Integrated Vision: Proceedings of the Sixth International Symposium on Life-Cycle Civil Engineering (IALCCE 2018), 28–31 October 2018, Taylor & Francis, Ghent, Belgium, 2018, pp. 965–972, https://doi.org/10.1201/9781315228914.
[12] C. Arya, F.K. Ofori-Darko, Influence of crack frequency on reinforcement corrosion in concrete, Cem. Concr. Res. 26 (1996) 345–353, https://doi.org/10.1016/S0008-8846(96)85022-8.
[13] O. Gautefall, O. Vennesland, Effect of cracks on the corrosion of embedded steel in silica concrete compared to ordinary concrete, Nordic Concr. Res. 2 (1983) 17–28.
[14] N.S. Berke, M.P. Dallaire, M.C. Hicks, R.J. Hoopes, Corrosion of steel in cracked concrete, Corrosion 49 (1993) 934–943.
[15] R. François, G. Arliguie, Effect of microcracking and cracking on the development of corrosion in reinforced concrete members, Mag. Concr. Res. 51 (1999) 143–150, https://doi.org/10.1680/macr.1999.51.2.143.
[16] H.E. Sørensen, S.L. Poulsen, U. Jönsson, Chloride threshold values from concrete blocks exposed at Rødbyhavn field exposure site, Full text available at:, in: H. D. Beushausen (Ed.), Performance-Based Approaches for Concrete Structures (14th Fib Symp.), RSA, Cape Town, 2016 https://www.researchgate.net/publication/318420354.
[17] I. Andersen, Salt- og temperaturforhold i de indre danske farvande (Salt and temperature conditions in the inner Danish waters), in: Technical Report No. 94-4, Danish Meteorological Institute, Copenhagen, 1994.
[18] L.A. Feldkamp, L.C. Davis, J.W. Kress, Practical cone-beam algorithm, J. Opt. Soc. Am. A 1 (1984) 612–619, https://doi.org/10.1364/JOSAA.1.000612.
[19] T. Danner, K. Hornbostel, Ø. Strømme, M.R. Geiker, Available at:, in: Self-healing and Chloride Ingress in Cracked Cathodically Protected Concrete Exposed to Marine Environment for 33 Years, NTNU, Trondhiem, Norway, 2019, p. 31 https://ntnuopen.ntnu.no/ntnu-xmlui/handle/11250/2631863.
[20] T. Danner, U. Hjorth Jakobsen, M.R. Geiker, Mineralogical sequence of self-healing products in cracked marine concrete, Minerals 9 (2019) 284, https://doi.org/10.3390/min9050284.
[21] T. Danner, M.R. Geiker, Long-term influence of concrete surface and crack orientation on self-healing and ingress in cracks – field observations, Nordic Concr. Res. 58 (2018) 1–16, https://doi.org/10.2478/ncr-2018-0001.
[22] U.H. Jakobsen, K. De Weerdt, M.R. Geiker, Elemental zonation in marine concrete, Cem. Concr. Res. 85 (2016) 12–27, https://doi.org/10.1016/j.cemconres.2016.02.006.
[23] S. Fjendbo, H.E. Sørensen, K. De Weerdt, U.H. Jakobsen, M.R. Geiker, Correlating the development of chloride profiles and microstructural changes in marine concrete up to ten years, Cem. Concr. Compos. 131 (2022), 104590, https://doi.org/10.1016/j.cemconcomp.2022.104590.
[24] V. Marcos-Meson, M. Geiker, G. Fischer, A. Solgaard, U.H. Jakobsen, T. Danner, C. Edvardsen, T.L. Skovhus, A. Michel, Durability of cracked SFRC exposed to wet-dry cycles of chlorides and carbon dioxide – multiscale deterioration phenomena, Cem. Concr. Res. 135 (2020), 106120, https://doi.org/10.1016/j.cemconres.2020.106120.
[25] U.M. Angst, M.R. Geiker, M.C. Alonso, R. Polder, O.B. Isgor, B. Elsener, H. Wong, A. Michel, K. Hornbostel, C. Gehlen, R. François, M. Sanchez, M. Criado, H. Sørensen, C. Hansson, R. Pillai, S. Mundra, J. Gulikers, M. Raupach, J. Pacheco, A. Sagüés, The effect of the steel–concrete interface on chloride-induced corrosion initiation in concrete: a critical review by RILEM TC 262-SCI, Mater. Struct. 52 (2019) 88, https://doi.org/10.1617/s11527-019-1387-0.
[26] E. Laursen, Betons reelle holdbarhed, Beton i Storebæltsforbindelsen, Sund & Bælt A/S, Presentation at Dansk Betonforening, Copenhagen, 18th November 2009, Danish Concrete Association, 2009.